







Deciphering the explosion mechanism of Type Ia SNe using their remnants II: a deep dive into double detonations with SNR 0509-67.5

SOHAM MANDAL ^{1,2} PARVIZ GHAVAMIAN ³ PRIYAM DAS ⁴ IVO ROLF SEITENZAHL ⁵
SHAZRENE MOHAMED ^{1,2,6,7,8} AND ASHLEY J. RUITER ⁴

¹*Department of Astronomy, University of Virginia, 530 McCormick Road, Charlottesville, VA 22904, USA*

²*Virginia Institute for Theoretical Astronomy, University of Virginia, Charlottesville, VA 22904, USA*

³*Department of Physics, Astronomy and Geosciences, Towson University, Towson, MD, 21252; pghavamian@towson.edu*

⁴*School of Science, The University of New South Wales, Australian Defence Force Academy, Northcott Drive, Campbell, Canberra, ACT 2600, Australia*

⁵*Mathematical Sciences Institute, Australian National University, Canberra, ACT 0200, Australia*

⁶*South African Astronomical Observatory, P.O Box 9, Observatory, 7935, Cape Town, South Africa*

⁷*Department of Astronomy, University of Cape Town, Private Bag X3, Rondebosch, 7701, Cape Town, South Africa*

⁸*NITheCS National Institute for Theoretical and Computational Sciences, South Africa*

ABSTRACT

Type Ia supernovae (SNe) occur when a white dwarf (WD) explodes via runaway thermonuclear burning. Till date, major uncertainties remain regarding the nature of the explosion mechanism and its observable signatures. In this work, we study how the ‘double detonation’ explosion mechanism, or a helium shell detonation in a sub-Chandrasekhar WD followed by a core detonation, shapes supernova remnants (SNRs) and encodes information about the WD progenitor. We evolve a suite of double-detonation SN models to the remnant phase, up to several centuries after explosion, and measure the characteristic sizes of substructures formed in the SNR due to turbulent mixing. By comparing our models to high-resolution optical observations of the young Type Ia SNR 0509–67.5, we find that the size distribution of its small-scale substructures is consistent with a double detonation explosion mechanism and further places constraints on the carbon–oxygen core mass and helium shell mass of the WD progenitor. The observed sizes of iron-dominated and sulfur-dominated substructures in SNR 0509–67.5 indicate a progenitor core mass and a shell mass of $1M_{\odot}$ and $\gtrsim 0.05M_{\odot}$, respectively.

Keywords: hydrodynamics — shock waves — supernova remnants — hydrodynamic instabilities — thermonuclear supernovae

1. INTRODUCTION

Type Ia supernovae (SNe Type Ia) are runaway thermonuclear explosions of white dwarf (WD) stars assumed to be rich in carbon and oxygen. They constitute an important pathway to the formation of elements in the present-day universe (and are the dominant source of iron-group elements; see Maoz & Graur 2017). They are regarded as crucial distance indicators in the cosmological distance ladder (Kirshner 2010), owing to their famous characteristic of having absolute luminosities that are tightly correlated with the width of their lightcurves

(Phillips 1993; Phillips & Burns 2017)¹. This is partly the reason why Type Ia SNe have been traditionally regarded as members of a homogenous population. Conventionally, Type Ia SNe were thought to occur when a carbon oxygen WD approaches the Chandrasekhar mass limit (M_{ch} ; Chandrasekhar 1931) via accretion. The near-Chandrasekhar mass (near- M_{ch} henceforth) WD becomes degenerate and thus cannot cool adiabatically in response to continued mass accretion. As a result its central density and temperature increases dramatically, leading to runaway nuclear burning and explosion of the WD (Arnett 1969; Hansen & Wheeler 1969; Nomoto 1982; Ruiter & Seitzzahl 2025).

¹ albeit more modern studies find that $\sim 30\%$ of SNe Type Ia do not follow this correlation (Taubenberger 2017).

Early models considered the expanding nuclear flame front to be either strictly subsonic or strictly supersonic; called deflagration (Nomoto et al. 1984; Iwamoto et al. 1999) and detonation (Arnett 1969; Hansen & Wheeler 1969), respectively. Pure detonation models exhibited very high explosion energies, along with overproduction of iron-group elements (IGEs) and underproduction of intermediate mass elements (IMEs), all of which are in conflict with observations (Arnett et al. 1971). The deflagration models, on the other hand, suffered from low ejecta kinetic energy and production of lower ^{56}Ni than is required to explain normal Type Ia SNe (Niemeyer et al. 1996; Niemeyer & Woosley 1997). The “delayed detonation” class of models were proposed to address this issue. In these models, nuclear burning initiates near the center of a near- M_{ch} WD as a subsonic flame. It later transitions to develop a supersonic combustion front, or detonation (Ivanova et al. 1974; Khokhlov 1991a,b). A popular example of this class is the deflagration-to-detonation transition model (DDT; see review by Röpke 2017).

Despite the success of these models, the idea of near- M_{ch} WDs being progenitors of Type Ia SNe were found to suffer from two major issues: they are less abundant in nature compared to their sub- M_{ch} counterparts (Kepler et al. 2007; Torres et al. 2021), and stable growth of WD masses to near- M_{ch} values requires rather finely-tuned accretion (Nomoto et al. 2007). This led to the suggestion that sub- M_{ch} WDs could also give rise to Type Ia SNe. This is called the double detonation (DD) model, in which a near-surface detonation occurs in the accreted helium shell of a sub- M_{ch} WD. This detonation sends a shockwave into the core of the WD, causing a second detonation and a subsequent thermonuclear runaway (Livne 1990; Woosley & Weaver 1994; Fink et al. 2007, 2010; Shen & Bildsten 2014; Polin et al. 2019). Another possible channel for Type Ia SNe from sub- M_{ch} WDs is the violent merger of two sub- M_{ch} WDs, followed by carbon ignition near the core of one of the WDs (Pakmor et al. 2010, 2012).

Both near- M_{ch} and sub- M_{ch} WD progenitors are now thought to be needed to explain the range of specific properties of observed Type Ia SNe, such as ejecta mass derived from lightcurve modeling (Scalzo et al. 2014; Bora et al. 2024), Mn/Fe ratio (Seitenzahl et al. 2013; Lach et al. 2020), nebular spectra-inferred Fe/Ni ratio (Flörs et al. 2020) and lightcurve-inferred $^{57}\text{Ni}/^{56}\text{Ni}$ ratio (Seitenzahl et al. 2009; Röpke et al. 2012; Tiwari et al. 2022), with most of the proposed explosion mechanisms likely at play. Perhaps then, it is not surprising that we have moved from the ‘homogenous family of lightcurves’ paradigm to a much more diverse fam-

ily of Type Ia lightcurves and spectra (Taubenberger 2017; Gal-Yam 2017), especially with the advent of modern high-cadence surveys such as the Palomar Transient Factory (PTF; Law et al. 2009), the All-Sky Automated Survey for SuperNovae (ASAS-SN; Kochanek et al. 2017), the Zwicky Transient Facility (ZTF) Bright Transient Survey (Perley et al. 2020), the Young Supernova Experiment (YSE; Aleo et al. 2023), the Dark Energy Survey (DES Collaboration et al. 2024), and the upcoming Legacy Survey of Space and Time (LSST; Ivezić et al. 2019). However, no clear correspondence between observed properties of Type Ia SNe spectra or lightcurves and the proposed thermonuclear explosion mechanisms has been discovered yet (Hillebrandt et al. 2013; Ruiter & Seitenzahl 2025).

Some studies have approached this problem from a different direction, that is, studying remnants of Type Ia SNe to identify the signatures of the mechanism responsible for the explosion (Badenes et al. 2006; Seitenzahl et al. 2019; Ferrand et al. 2021; Mandal et al. 2025). A specific example of such a signature is the presence of a large-scale conical ‘shadow’ in the ejecta of a Type-Ia SNR that exploded via the DD channel in the presence of another WD (Ferrand et al. 2022).

An ideal candidate for this line of investigation is the well-studied supernova remnant (SNR) 0509-67.5, located in the Large Magellanic Cloud (LMC). SNR 0509-67.5 (henceforth 0509) has been observed extensively in radio (Bozzetto et al. 2014), infrared (Seok et al. 2013), optical (Helder et al. 2010; Hovey et al. 2015), UV (Ghavamian et al. 2007) and X-ray bands (Warren & Hughes 2004; Kosenko et al. 2008). The light echo spectrum of 0509 suggests that it belongs to the class of overluminous, slowly fading, 1991T-like SNe (Rest et al. 2008). 1D hydrodynamic models with detailed non-equilibrium ionization calculations (Badenes et al. 2008) also support this conclusion, showing that both the dynamics and the X-ray line flux ratios for 0509 are most consistent with a highly energetic and luminous SN akin to SN 1991T (Phillips et al. 2022, 2024). Hydrodynamics-based Bayesian analysis of the kinematics of 0509 as revealed by the Hubble Space Telescope (Arunachalam et al. 2022) suggest a large value of explosion energy ($\sim 1.3 \times 10^{51}$ erg), again favoring a 1991T spectral subtype for this Type Ia SNR. In addition to spectral classification, Badenes et al. (2008) also show that 1D delayed detonation (DDT) explosion of near- M_{ch} WDs are a good match for 0509. Yet another possibility is an SN explosion within a planetary nebula (Soker 2025).

On the other hand, Seitenzahl et al. (2019) argue in favor of a sub- M_{ch} WD explosion. They obtain high-

resolution optical observations that reveal highly ionized Fe clumps in 0509. Using detailed time-dependent ionization balance calculations based on analytic SNR models (Truelove & McKee 1999), they find that the dynamics and strongly ionized state of the Fe clumps make 0509 most consistent with a $1M_{\odot}$ WD explosion, although a near- M_{ch} WD explosion with unburnt He in the ejecta cannot be ruled out. They also favor a large explosion energy ($\approx 1.5 \times 10^{51}$ erg) and note that this energy is available via detonation of a WD with a $0.85M_{\odot}$ carbon-oxygen (CO) core and a $0.15M_{\odot}$ helium (He) shell. Recent optical tomography of 0509 from the deep MUSE (Multi Unit Spectroscopic Explorer) data revealed a double shell [Ca XV] and a single shell [S XII] morphology in the ejecta (Das et al. 2025). Their study suggested that this signature can be expected from the double detonation of a CO WD with $\sim 1M_{\odot}$ core and a helium shell of $\sim 0.03M_{\odot}$.

Despite the growing evidence for a sub- M_{ch} WD progenitor for 0509, sub- M_{ch} models have generally been considered poor matches to the 1991T-like spectral subtype. Very high peak luminosities ($M_B < -19.5$ mag) and slow decline rates ($\Delta m_{15}[B] = 0.95 \pm 0.05$) are exhibited by 1991T-like SNe (Phillips et al. 2022, 2024), implying large ^{56}Ni yields ($1.0 - 1.4M_{\odot}$; see Filippenko et al. 1992). Typically, sub- M_{ch} explosion models produce less ^{56}Ni ($0.3 - 0.8M_{\odot}$; e.g., Sim et al. 2010) owing to their lower central densities. Although double detonation models were proposed to explain the peculiar Fe absorption features in pre-maximum phase optical spectra of 1991T-like SNe (Filippenko et al. 1992), more recent studies have identified tensions between spectral properties of sub- M_{ch} models and 1991T-like SNe. In particular, the peak B-band magnitude (M_B) and high Si II velocities favor a near- M_{ch} origin (Polin et al. 2019, 2021), and double detonation models tend to overproduce the [Ca II]/[Fe III] ratio in the optical nebular spectra of luminous (including 1991T-like) SNe (Polin et al. 2021).

SNR 0509 provides us an unparalleled opportunity to probe the tension between 1991T-like SNe and DD models, in a way that cannot be pursued with early time SNe. This is due to the fact that SNR 0509 is in a late enough stage of evolution for its ejecta structure to be spatially resolved (~ 400 yrs; Rest et al. 2005) unlike early time SNe, but not evolved enough for its ejecta to have mixed substantially with gas from the interstellar medium (ISM). This allows us to use a recent result by Mandal et al. (2025), who show that the typical size of small-scale substructures in Type Ia SNRs with sub- M_{ch} WD progenitors depend strongly on their composition. These substructures originate from

turbulence in the SNR, which becomes susceptible to hydrodynamic instabilities (Rayleigh-Taylor Instability and Kelvin-Helmholtz Instability) as it expands against the ambient medium (Chevalier & Klein 1978; Chevalier et al. 1992). The size distribution of these substructures bear signatures of the outermost layers of the stellar ejecta (Polin et al. 2022; Mandal et al. 2023).

This study builds directly on the method proposed by Mandal et al. (2025), focusing on Type Ia SNRs originating from a double detonation explosion. We develop a suite of three-dimensional double detonation SNR models with a range of progenitor masses and obtain substructure size distributions as a function of time for each model. We then analyze optical coronal line maps (forbidden line emission from highly ionized atoms; see Seitzzahl et al. 2019) of SNR 0509 (Fig. 1) and compare the resulting substructure morphologies with those of our numerical models. This provides an application of the method of Mandal et al. (2025) to a well-observed remnant. It yields an independent morphological test of the explosion mechanism of 0509, complementary to the analysis of element distributions by Das et al. (2025). It also allows us to place constraints on the core and shell masses of the progenitor WD.

This work is organized as follows: The observational data used in this work are described in Section 2. Details of the SNR models and the techniques used to analyze the models and the data are discussed in Section 3. The results are presented in Section 4, and a summary of the results is presented in Section 5.

2. OBSERVATIONAL DATA

A deep observational campaign targeting the supernova remnant SNR 0509 was carried out using the Multi Unit Spectroscopic Explorer (MUSE; Bacon et al. 2010), an optical integral field spectrograph mounted on Unit Telescope 4 (UT4) of the European Southern Observatory’s (ESO) Very Large Telescope at Cerro Paranal. This effort was part of ESO program 0104.D-0104(A), led by P.I. Seitzzahl. Observations were conducted in service mode using the Wide Field Mode with Adaptive Optics (WFM-AO) configuration, spread over 25 nights across a 24-month period (see Methods in Das et al. 2025). A total of 40 exposures were obtained: 39 of these were approximately 2700 seconds in duration, while one shorter observation lasting 93.92 seconds was discarded due to poor data quality. The resulting dataset comprises a total exposure time of roughly 105,300 seconds (equivalent to 29 hours and 15 minutes). Each MUSE data cube covers the optical wavelength range from 4690 \AA to 9340 \AA at a spectral resolution of $R \sim 3000$. To minimize contamination from the

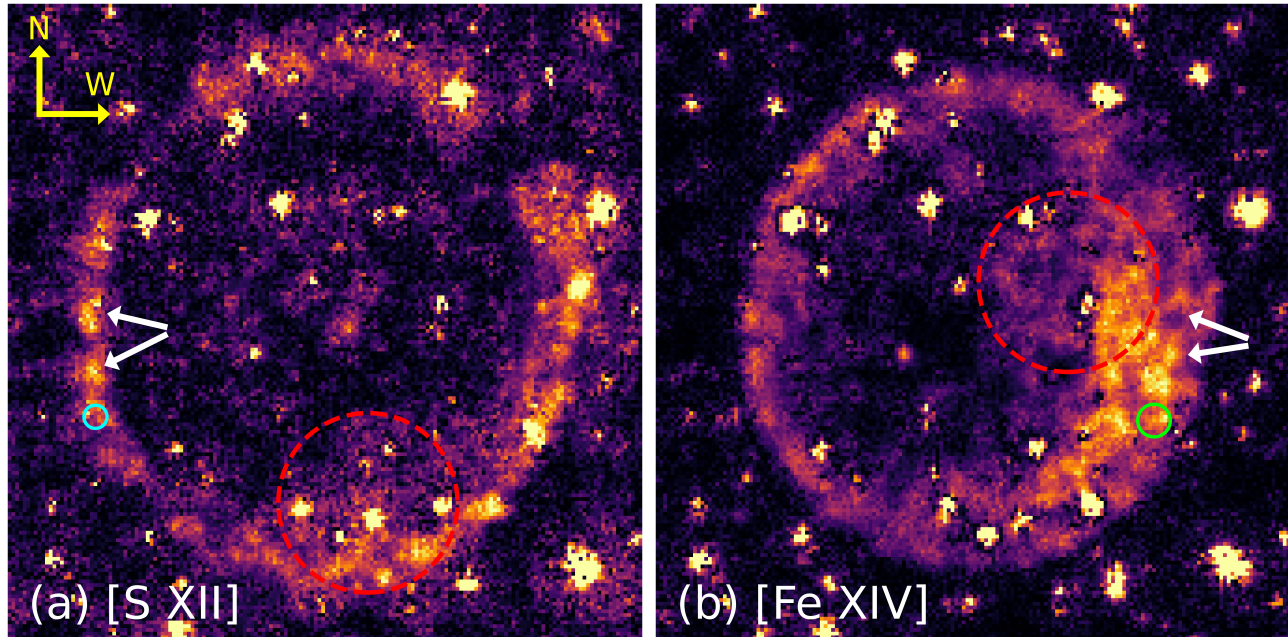


Figure 1. [S XII] (*left*) and [Fe XIV] (*right*) emissivity distributions in SNR 0509-67.5. Circles corresponding to spherical harmonics $l \approx 30$ (solid cyan) and $l \approx 20$ (solid green) are overlaid on the S and Fe images, respectively. A circle of radius corresponding to $l = 4$ (dotted red) is also marked on both images. These harmonics correspond to bends in the power spectra of 0509 (shown in Fig. 3) and likely to the small scale substructures in these images. White arrows overlaid on the plots point to some examples of these substructures.

laser guide stars of the 4LGSF system, a notch filter is employed in WFM-AO mode to block the spectral region from 5804 \AA to 5965 \AA (Vogt et al. 2018; Vogt et al. 2017). However, this filter does not completely eliminate the effects of Raman-scattered photons originating from the laser light. These residual artifacts are subsequently identified and removed during data processing using the MUSE data reduction pipeline (Weilbacher et al. 2020).

Data reduction was performed using ESOReflex (Freudling et al. 2013) version 2.11.5 and the MUSE data reduction pipeline version 2.8.9 (Weilbacher et al. 2020), both run with default settings. The process included the removal of known sky lines and was carried out on Tycho, a high-memory Linux workstation at the University of New South Wales in Canberra, specifically configured for handling MUSE data. Since no dedicated sky observations were available, background subtraction was performed using the pipeline’s alternative method: computing a sky model from a specified portion of the field of view, controlled by the parameter SkyFr.2. All individual data cubes were stored in a single directory, used as the pipeline’s input (with no additional calibration files). The final mosaic was produced by re-running the pipeline with the 39 reduced MUSE pixel tables as input, combining them into a single data cube. This mosaic covers a $1' \times 1'$ field of view, with a spatial sampling

of $0.2'' \times 0.2''$ per spaxel, and was used for all subsequent analysis.

For this work, we choose the [Fe XIV] $\lambda 5303 \text{ \AA}$ on account of being the brightest of all the coronal lines and [S XII] $\lambda 7611 \text{ \AA}$ for being the brightest non-iron coronal line. Das et al. (2025) provide a representative spectrum for 0509 (extracted from a region on its western side; see their Fig. 1). However, the overall surface brightness of the [Fe XIV] $\lambda 5303 \text{ \AA}$ and [S XII] $\lambda 7611 \text{ \AA}$ lines is much lower than that of $H\alpha$, which is dominated by strongly limb-brightened Balmer filaments along the outer rim of the remnant. Hence, conventional background subtraction was found to be insufficient. The final mosaic data cube was thus processed with an additional background subtraction and galactic de-reddening (Das et al. 2025; Ghavamian et al. 2017, see details).

[Fe XIV] $\lambda 5303 \text{ \AA}$ and [S XII] $\lambda 7611 \text{ \AA}$ emission are visualized by integrating the spectra over specific wavelength intervals (λ_1 and λ_2) corresponding to the emission features of each forbidden line. To remove the underlying stellar continuum, adjacent spectral regions on either side of the emission line ($\Delta\lambda_{*1}$ and $\Delta\lambda_{*2}$) are also integrated and subtracted from the signal. The chosen wavelength ranges for both the emission features and the surrounding continua are listed in Table 1.

3. NUMERICAL METHOD

Table 1. Spectral windows used to remove stellar continuum and isolate emission from ionized species.

Coronal Emission Lines	$\lambda_1(\text{\AA})$	$\lambda_2(\text{\AA})$	$\Delta\lambda_{*1}(\text{\AA})$	$\Delta\lambda_{*2}(\text{\AA})$	Peak Surface Brightness ($\text{ergs}^{-1}\text{cm}^{-2}\text{arcsec}^{-2}$)
[Fe XIV]	5218	5364	5150 - 5190	5485 - 5528	6.77×10^{-17}
[S XII]	7602	7705	7393 - 7484	7779 - 7809	2.67×10^{-17}

3.1. Initial conditions

We use angle-averaged (1D) versions of DD models described in Gronow et al. (2021), hosted on the HESMA project (Kromer et al. 2017) website². These models span a range of CO core masses and He shell masses. The details of these models are listed in Table 2. The angle-averaged profiles reproduce the radial distribution of mass and composition in the ejecta but do not retain the asymmetries intrinsic in the original 3D explosion models. Studies that follow fully three-dimensional supernova models into the remnant phase have shown that such explosion-imprinted anisotropies primarily influence the global morphology of the remnant, corresponding to the lowest spherical harmonic modes ($l \lesssim 10$), whereas the structures at intermediate and smaller angular scales arise mainly from hydrodynamic instabilities that develop as the remnant evolves (Ferrand et al. 2019, 2021).

Additional tests presented by Mandal et al. (2023) examined how perturbations introduced in the ejecta (or the ambient medium) propagate during remnant evolution. These calculations show that initially imposed perturbations do not typically produce identifiable features in the power spectrum for long. Instead, within a few decades the structure of the remnant becomes governed by Rayleigh–Taylor instability growth at the contact discontinuity. Because the present study focuses on the statistical properties of structures that emerge during the SNR phase (several centuries after the explosion), we do not expect the omission of explosion-imprinted perturbations in the initial conditions to significantly influence the measured power spectra.

The ejecta density profile and abundance profiles for S and Fe from the SN models are mapped onto a 3D domain and allowed to expand to the SNR phase (described in the next Section). The ejecta are assumed to be cold ($P = 10^{-6}\rho$) and expanding homologously ($v = r/t$). The ambient medium is set to have uniform density. Using spherically symmetric initial conditions

Table 2. Summary of the DD SN models used in this work.

Name	Core mass (in M_{\odot})	Shell mass (in M_{\odot})	Explosion energy (in 10^{51} erg)
M0803	0.8	0.03	0.75
M0805	0.8	0.05	0.84
M0903	0.9	0.03	0.97
M0905	0.9	0.05	1.05
M0910	0.9	0.10	1.50
M1003	1.0	0.03	1.44
M1005	1.0	0.05	1.42
M1010	1.0	0.10	1.48

also allows us to model only one octant of the remnant (as in Mandal et al. 2023) without introducing additional nonphysical symmetries, enabling higher effective resolution than would be practical for a full-sphere simulation at comparable computational cost.

3.2. Remnant evolution and analysis

The 1D models are mapped onto a 3D Cartesian grid in *Sprout*, a second-order ideal hydrodynamics code (Mandal & Duffell 2023) designed to studying expanding outflows. *Sprout* utilizes the moving mesh paradigm (Springel 2010; Duffell & MacFadyen 2011) to expand its computational domain with time, following the evolution of the SNR. The expanding grid provides a high dynamic range in resolution. This is necessary to model the SNR’s expansion, which starts at 100s and continues till 600 yrs. The end time is chosen keeping in mind the age estimate of SNR 0509-67.5, which is roughly in the range 300 – 500 yrs (Rest et al. 2005; Hovey et al. 2015).

It is convenient to describe the time evolution of the SNR models in terms of a dimensionless quantity t_D , called the dynamical age of the remnant. This is essentially the age of the remnant (t) divided by the characteristic time or Sedov time (T_c), which is the time taken by the forward shock to sweep up mass comparable to the ejecta mass itself. The characteristic time

² <https://hesma.h-its.org>

is a function of the ejecta mass M , explosion energy E , and ambient medium (AM) density (Truelove & McKee 1999; Warren & Blondin 2013; Mandal et al. 2024). Using this, we can define the dynamical age t_D as follows:

$$t_D \equiv \left(\frac{t}{628 \text{yrs}} \right) \left(\frac{M}{M_{ch}} \right)^{5/6} E_{51}^{-1/2} n_0^{-1/3}, \quad (1)$$

where $M_{ch} = 1.4M_\odot$ is the Chandrasekhar mass, $E_{51} = E/(10^{51} \text{ergs})$, and n_0 is the AM density in units of amu cm^{-3} . Note that this definition is not unique. For example, Warren & Blondin (2013) choose a different characteristic age T' , which is related to our choice as $T' = 0.43T_c$.

We compute power spectra of these 3D models at several instants of time, using the method outlined in Polin et al. (2022) and Mandal et al. (2023). Since the computations evolve only one octant of the remnant, the data for each model snapshot is reflected across the coordinate planes to reconstruct a full spherical remnant. This imposed symmetry affects only the lowest multipoles, which are not used in the present analysis. Spherical surface distributions of the radially integrated density distributions of S (and Fe) are then calculated for each reconstructed snapshot as follows:

$$\langle \rho_S \rangle (\theta, \phi) = \frac{\int X_S P \rho dr}{\int X_S P dr}, \quad (2)$$

where X_S is the passive scalar representing the mass fraction of S. These spherical surface distributions are expanded in terms of spherical harmonics using the SHTOOLS package (Wieczorek & Meschede 2018). This allows us to derive a power spectrum C_l in terms of the spherical harmonic l (see Eqns. 11 and 12 of Mandal et al. 2024). Weighting by the product of pressure and the relevant passive scalar (tracing S or Fe ejecta) ensures that only the shocked, turbulent ejecta contributes to this calculation. Within the region between the forward and reverse shocks, this product varies by at most a factor of $\lesssim 1.5$, so the weighting does not strongly bias the calculation toward localized high-pressure regions. To verify that our results are not sensitive to the precise weighting prescription, we repeat the analysis using a constant weight for all cells above a pressure threshold. Power spectra derived from the spherical surface maps for each case are found to be nearly identical.

Our models utilize discretization errors associated with the Cartesian grid to provide seed perturbations to the contact discontinuity, which rapidly becomes unstable and exhibits growth of turbulent substructures. As found by Polin et al. (2022) and Mandal et al. (2023), the nature of seed perturbations (whether inherent to the grid or imposed externally) does not appreciably af-

fect the growth of turbulence in SNRs. Mandal et al. (2023) further show (in their Appendix) that grid-scale features typically appear in the power spectrum of SNR models at very large spherical harmonics ($l \sim 1000$ for a grid with 512 cells per dimension) and do not interfere with the lengthscales that correspond to the typical size of turbulent substructures ($l \lesssim 100$). Following Mandal et al. (2023), we adopt a resolution of 512^3 cells for our computational grid to ensure minimal influence of grid-scale noise on the power spectra.

3.3. Image analysis

The substructure size distributions in the images of 0509 are measured using the Δ -variance algorithm (Arévalo et al. 2012), as adapted by Mandal et al. (2024). This technique computes a low resolution power spectrum of a two-dimensional image, as is the case here. It is to be noted that this power spectrum is not necessarily equivalent to those of 3D models we describe in Section 3.2. However, Mandal et al. (2024) showed that power spectra of their 3D SNR models are equivalent to the Δ -variance-based power spectra of synthetic images corresponding to the same models, for spherical harmonics $l \gtrsim 10$. This equivalence provides the foundation for our analysis. We thus interpret the Δ -variance-derived power spectra of 0509 as representative of the underlying 3D ejecta distribution and directly compare them to the power spectra of our 3D models.

Since Δ -variance computes power as a function of lengthscale σ (in pixel units), it has to be converted to the angular harmonic l as shown by Mandal et al. (2024):

$$l \approx 1.6R_{\text{SNR}}/\sigma, \quad (3)$$

where R_{SNR} is the radius of the image of the SNR, also in pixel units. We apply masks on the field stars to ensure they are not contaminating our analysis.

4. RESULTS

4.1. Power spectral analysis of numerical models

Power spectra of hydrodynamic SNR models without large scale asymmetries are expected to have a broken power-law form (Warren & Blondin 2013; Polin et al. 2022; Mandal et al. 2023)³:

$$C_l \propto \frac{1}{(l/l_0)^{-n_1} + (l/l_0)^{n_2}}, \quad (4)$$

where l_0 is the wavenumber at which the power spectrum peaks. The power spectra can be approximated at

³ There can be deviations from this shape if large scale asymmetries are present, see Ferrand et al. (2021) for examples.

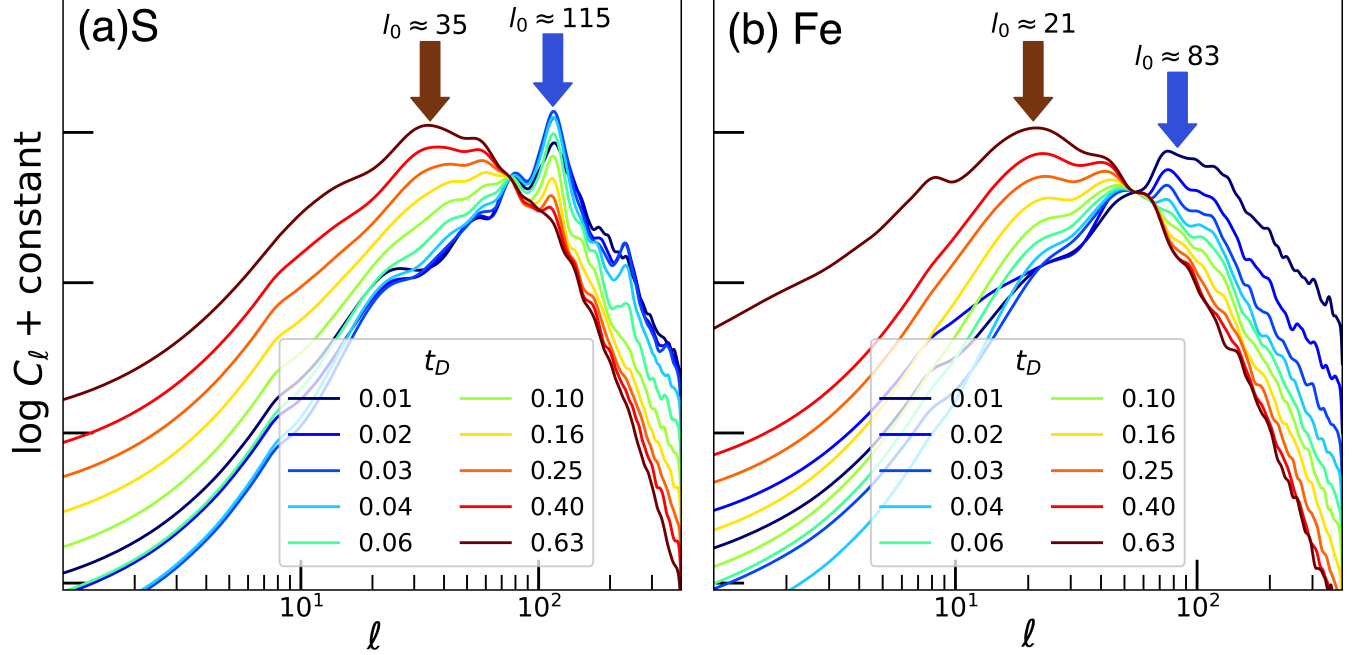


Figure 2. Power spectrum of S (*left*) and Fe (*right*) distributions in the ejecta of the M1003 model, evaluated at 10 logarithmically spaced time instants in the range $t_D = 0.01 - 0.63$. All power spectra have a broken power-law shape. The wavenumber where the power spectrum changes slope or peaks (l_0) corresponds to the lengthscale where most of the power in the turbulent substructures reside. With time, l_0 shifts to smaller values, indicating growth of the turbulent substructures. For DD SNRs, l_0 of S distribution (l_0^S henceforth) consistently remains larger than the l_0 for Fe distribution (l_0^{Fe} henceforth). For example, at $t_D = 0.01$, $l_0^S \approx 115$, while $l_0^{\text{Fe}} \approx 83$. The overall normalization for each power spectrum were chosen arbitrarily, to aid visual inspection and easy identification of l_0 .

$l \lesssim l_0$ as $C_l \propto l^{n_1}$, and at $l \gtrsim l_0$ as $C_l \propto l^{-n_2}$, with n_1 and n_2 being positive. The peak wavenumber l_0 corresponds to the typical size of the turbulent eddies formed in the ejecta-AM interaction of the SNR.

Our double detonation SNR models show a similar behavior. In Fig. 2, we plot the power spectra of S (left panel) and Fe (right panel) distributions in the M1003 model at various instants of time. The power spectra of S and Fe represent those of IMEs and IGEs, respectively. The overall normalization of each power spectrum is arbitrary and were chosen to aid visual inspection. Power spectra at early times are plotted in blue, and the colors transition to red at late times. For both panels, l_0 decreases with time, that is, the peak shifts to the left. This behavior can be understood by noting that l_0 is roughly proportional to the effective power-law slope of the ejecta encountered by the reverse shock (Polin et al. 2022; Mandal et al. 2023). This result suggests that the typical size of turbulent eddies in SNRs is of the order of the density scale height at the reverse shock. Since the ejecta density falls off steeply at large radii but is relatively shallow in the inner regions (for an example, see Fig. 2 of Collins et al. 2025), the reverse shock encounters shallower density profiles as it moves deeper into the ejecta. Thus the value of the ejecta power-law

slope encountered by the reverse shock decreases with age.

The value of l_0 thus allows us to constrain the dynamical age of an SNR, as will be further demonstrated in section 4.3. It is also possible to measure l_0 from the density distribution of the ejecta (not differentiating between elements) and estimate the dynamical age of the SNR (Mandal et al. 2024, 2025). Moreover, Fig. 2 shows that the value of l_0 for the power spectrum of IMEs (l_0^S henceforth) is seen to be greater than the value of l_0 for the power spectrum of IGEs (l_0^{Fe} henceforth) at every instant of time. This is an exclusive signature of SNRs with sub- M_{ch} WD progenitors (Mandal et al. 2025). This property stems from the fact that near- M_{ch} Type Ia SN progenitors generate a lot of buoyant ashes from their initial deflagration phase that cause significant mixing in the ejecta. The sub- M_{ch} WD progenitors are expected to experience detonations (or supersonic nuclear flame fronts) only, that do not cause this amount of mixing and therefore retain stratification in their ejecta. This causes the IMEs and IGEs to participate at different times in the ejecta-AM interaction and therefore develop substructures with different typical sizes (see Section 4.4 of Mandal et al. 2025). This

holds true for all our DD SNR models, as will be seen in section 4.3.

4.2. Substructure analysis of SNR 0509-67.5

The left panel of Fig. 3 shows the power spectra obtained from the [Fe XIV] and [S XII] images of 0509. Both spectra exhibit a pronounced peak at $l = 4$. A peak at low wavenumbers indicates substantial large-scale asymmetry in the SNR, consistent with the morphology seen in both our optical coronal line maps (Fig. 1) and X-ray images of 0509 (see panel 1 of Fig. 1 in Lopez et al. 2011). Using Eqn. 3, we illustrate the characteristic scale of the $l = 4$ peak by overlaying the Fe and S maps in Fig. 1 with a dotted red circle of the corresponding diameter, highlighting structures on comparable scales.

In addition to the large-scale asymmetry traced by the $l = 4$ peak, both power spectra exhibit clear breaks in slope at higher wavenumbers (marked with arrows in the left panel of Fig. 3). The Fe power spectrum shows a break near $l \approx 20$, while the S power spectrum displays a similar feature near $l \approx 30$. These wavenumbers correspond to smaller characteristic physical scales, indicative of compact substructures in 0509. Notably, a qualitatively similar spectral morphology has been reported for Tycho's SNR (Mandal et al. 2024, 2025), including the low- l peak and the higher- l break. Motivated by this correspondence, we associate these physical scales with turbulent substructures in 0509. To illustrate this possible correspondence, we overlay circles of the corresponding diameters on the 0509 images (Fig. 1). These broadly match the sizes of the observed small-scale substructures in 0509 (see, e.g., the alternately bright and dark circular patches in northwestern part of the Fe image in Fig. 1).

Motivated by the arguments above, we interpret the large- l power spectral breaks in 0509 as the turbulent peaks seen in the power spectra of our SNR models. According to this interpretation, each observed power spectrum may be described as the superposition of two components: a large-scale feature near $l \approx 4$ arising from large-scale intrinsic ejecta asymmetries, and a broken power-law component (as in Fig. 2 or Eqn. 4) associated with turbulent activity. To quantify the break wavenumbers, we therefore fit the Fe and S power spectra of 0509 with the sum of two broken power laws (each of the form given in Eq. 4), representing the asymmetry and turbulent contributions, respectively. For the power spectrum of S distribution, the fit provides $l_0 (= l_0^S) = 31 \pm 2$ and $n_2 = 2.16 \pm 0.05$. For the power spectrum of Fe distribution, the fit provides $l_0 (= l_0^{\text{Fe}}) = 22 \pm 1$ and $n_2 = 2.50 \pm 0.04$, with the quoted uncertainties corresponding to 1σ confidence intervals for either case.

Considering the radius of 0509 as observed in the sky is $\approx 15''$ (Arunachalam et al. 2022), we find the typical size of S and Fe dominated substructures seen in Fig. 1 to be $\approx 0.8''$ and $\approx 1.1''$ respectively (using Eqn. 3 and the values of l_0^S and l_0^{Fe}).

We find $l_0^S/l_0^{\text{Fe}} = 1.42 \pm 0.20$, that is, S dominated substructures in 0509 have a larger value of l_0 and thus a smaller typical size compared to their Fe dominated counterparts. This is exactly the signature of Type Ia SNRs with sub- M_{ch} progenitors found by Mandal et al. (2025), as mentioned in Section 4.1. In addition, both the S and Fe power spectra at small scales obey a power law $C_l \propto l^{-n_2}$, with $n_2 > 2$. This is much steeper compared to the power spectrum expected for a Kolmogorov-like turbulent cascade ($C_l \propto l^{-5/3}$; Kolmogorov 1941). Hence, 0509 also exhibits an absence of turbulent cascade at small scales that is typically seen in numerical SNR models (Polin et al. 2022; Mandal et al. 2024).

4.3. Trends in l_0^S and l_0^{Fe} of double detonation SNRs: implications for SNR 0509-67.5

In Fig 4, we plot the time evolution of l_0^S (top panel) and l_0^{Fe} (bottom panel) for all of our models. The general trend of l_0 decreasing with time is observed. In addition, all l_0 values asymptote to a minimum at late times, as also noted by Mandal et al. (2024). We also overlay the panels with the most likely range of l_0^S and l_0^{Fe} for 0509 (as obtained in Section 4.2), along with the possible range of dynamical age (t_D) of 0509, which has to be calculated using estimates of its age and Sedov time (T_c). The age of 0509 is estimated to be 400 ± 120 years from light echo modeling (Rest et al. 2005). A range of values for the Sedov time are calculated using the ejecta masses and the explosion energies of our SNR models, as provided in Table 2. This calculation also requires a value for the ambient density, which is taken to be 0.4 cm^{-3} , following Seitenzahl et al. (2019). Using the range of age and Sedov time estimates for 0509, we find its dynamical age to be in the range $t_D = 0.37 - 0.84$.

The top panel of Fig. 4 shows that the asymptotic value of l_0^S at late times is dependent upon the core mass. Models with lower core mass (M0803 and 0805; dashed lines) exhibit a lower asymptotic value of l_0^S in comparison to higher core mass models. In other words, lower core mass models tend to form larger IME clumps in comparison to their higher core mass counterparts. This trend is not monotonic, since the asymptotic value of l_0^S for the model M0903 is found to be greater than the same for the M10xx models, but a stark difference is found between the models with core mass above and

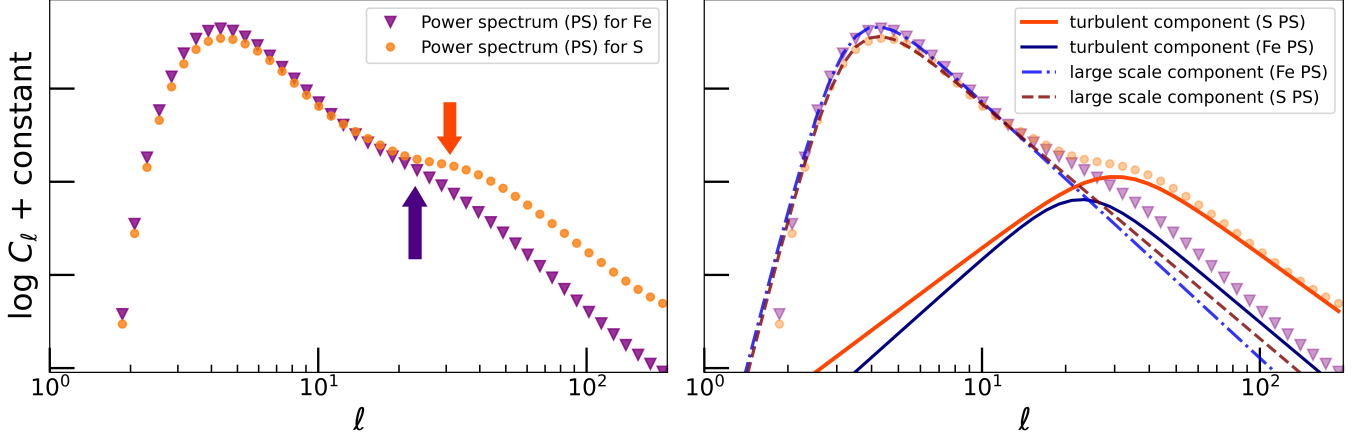


Figure 3. *Left.* Power spectra of S and Fe distributions in SNR 0509-67.5. Both power spectra show a strong bump at $l \approx 4$, which is anticipated given the presence of the prominent large scale asymmetric features in 0509. Both curves also show a bend or change in slope (at $l \approx 30$ and $l \approx 20$ for S and Fe respectively, marked by arrows in the plot). These spectral breaks likely correspond to small-scale substructures seen in 0509 (see Fig. 1). *Right.* Both power spectra are fit to a two-component model; one corresponding to low- l anisotropies in the ejecta, and the other signifying turbulent activity in the SNR at higher values of l (small-scale substructures).

below $0.8M_{\odot}$. In contrast, l_0^S isn't found to be sensitive to the mass of the He shell.

The bottom panel of Fig. 4 shows that the asymptotic value of l_0^{Fe} is lower than that of l_0^S for each model, as expected. It is also found that the asymptotic value of l_0^{Fe} increases with increasing core mass. Focusing on a particular value of core mass, one finds that the models with lower shell masses tend to have a larger asymptotic value of l_0^{Fe} (compare the l_0^{Fe} curves for M0803 and M0805, for example). Nevertheless, there is sufficient degeneracy in l_0^{Fe} due to the varying core masses of our models that it would be difficult to constrain the shell mass unless the core mass was known accurately.

Comparing the values of l_0^S in our models to those found for 0509, we find that models with mass $\leq 0.8M_{\odot}$ are not consistent with 0509. The only models favored by the l_0^S measurements are M0910 and M1010. The value of l_0^S measured for 0509 also restricts us to $t_D \gtrsim 0.7$, as can be seen from the top panel of Fig. 4. Looking at the range $0.70 < t_D < 0.84$ in the bottom panel of Fig. 4, we see that the measured value of l_0^{Fe} in 0509 favors the M0903, M1003, M1005, and M1010 models. We therefore conclude that M1010 is the model in our suite that best reproduces the observed values of both l_0^S and l_0^{Fe} in 0509 simultaneously. However, the late-time morphology of M0910 is also reasonably similar to that of 0509, with $l_0^S = 30\text{--}32$ and $l_0^{\text{Fe}} = 20$ for $t_D = 0.70\text{--}0.84$. The predicted l_0^S lies within the 1σ observational interval, while l_0^{Fe} differs from the measured value for 0509 by $\approx 2\sigma$. A discrepancy at this level does not constitute a statistically significant exclusion, but rather indicates that the model is disfavored relative to

M1010. Models with thinner He shells are more strongly inconsistent with the observations.

Taken together, the model comparisons indicate that 0509 is best explained by a DD explosion of a sub- M_{ch} WD with a relatively massive CO core and He shell, as required by both the successful model (M1010) and the marginally consistent model (M0910). Interpreted within the parameter space sampled by our model grid, this corresponds approximately to CO core masses of $0.9\text{--}1.0M_{\odot}$ and He shell masses in the range $0.05M_{\odot} < M \lesssim 0.1M_{\odot}$. A finer exploration of the CO core and He-shell mass parameter space would be required to determine tighter quantitative bounds.

We note that this constraint holds even if one estimates t_D for 0509 assuming a near- M_{ch} WD progenitor, unlike our calculation. For instance, Arunachalam et al. (2022) favor a near- M_{ch} origin for 0509, on the basis of forward shock kinematics measured using Hubble H α observations. Assuming $E_{51} = 1.4$, they obtain $M = 2.02 \pm 0.85M_{\odot}$, $\log \rho_0 = -24.23 \pm 0.09$, and an age of $t = 329.7 \pm 17.3$ years for 0509. Alternatively, holding M fixed to $1.4M_{\odot}$, they estimate probable ranges $E_{51} = 1.30 \pm 0.41$, $\log \rho_0 = -24.20 \pm 0.20$, and an age of $t = 317.19 \pm 12.95$ years. Using these values, we obtain a range of $t_D = 0.65\text{--}0.95$. As Fig. 4 shows, this range of t_D still favors the M1010 model when the values of both l_0^S and l_0^{Fe} are considered.

The M1010 model has an ejecta mass of $1.1M_{\odot}$ and kinetic energy $\approx 1.5 \times 10^{51}$ ergs. Also taking the age of 0509 to be 400 ± 120 years (Rest et al. 2005), we can compute a range of dynamical age for 0509 using Eqn. 1:

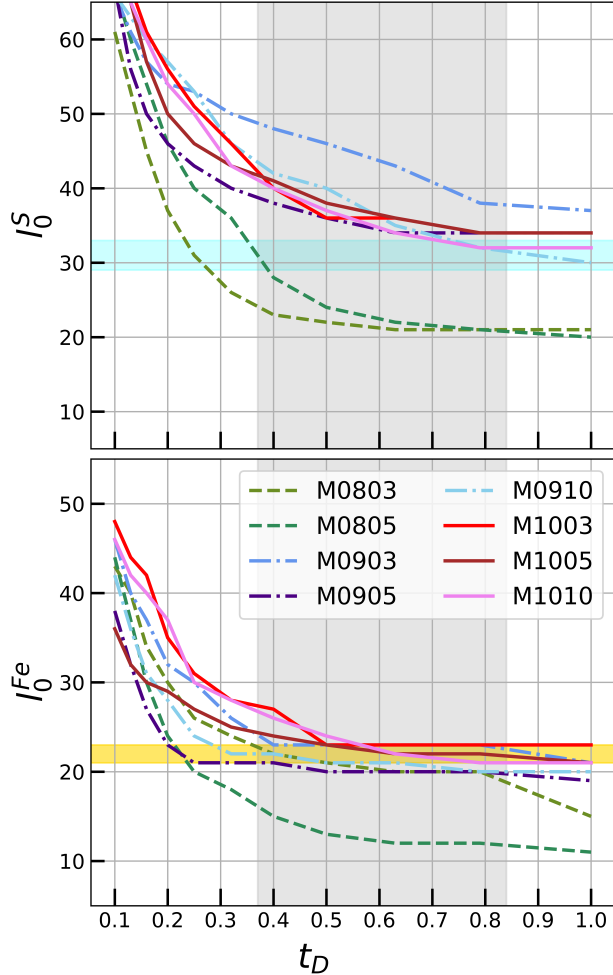


Figure 4. Evolution of l_0^S (top) and l_0^{Fe} (bottom) with time for all DD SNR models. Results for models with core masses of $0.8M_\odot$, $0.9M_\odot$ and $1.0M_\odot$ have been plotted with dashed, dash-dotted, and solid lines respectively for ease of viewing. These plots have been overlaid with the range of $l_0^S (= 31 \pm 2)$ and $l_0^{\text{Fe}} (= 22 \pm 1)$ obtained from our fit for the power spectra of 0509, along with the likely range of dynamical age (t_D) of 0509.

$$\begin{aligned}
 t_D &= \left(\frac{400 \pm 120 \text{yrs}}{628 \text{yrs}} \right) \left(\frac{1.1M_\odot}{1.4M_\odot} \right)^{5/6} 1.5^{-1/2} n_0^{-1/3} \\
 &= (0.43 \pm 0.13) n_0^{-1/3}.
 \end{aligned} \tag{5}$$

We can estimate the number density of the AM currently being encountered by the forward shock in 0509, by comparing Eqn. 5 to the range $0.70 < t_D < 0.84$ predicted by our analysis. This yields a range $0.05 < n_0 < 0.5$ (in units of cm^{-3}) for the AM density around 0509 today. This is a rather broad range, but is consistent with all previous estimates for the AM density around 0509 (Seitenzahl et al. 2019; Arunachalam et al. 2022).

An additional, independent test of the models is provided by the physical size of 0509, which has been constrained to ≈ 3.6 pc (Hovey et al. 2015; Arunachalam et al. 2022). Using the analytical framework of Truelove & McKee (1999), Seitenzahl et al. (2019) demonstrated that an ejecta mass of $1M_\odot$, explosion energy of 1.5×10^{51} ergs, and AM number density of 0.4cm^{-3} can reproduce this observed size. For the M1010 model (with mass and energy as listed in Table 2), the forward-shock radius is 3.45 pc at $t_D = 0.7$, in good agreement with the measured value. At later dynamical times (e.g., $t_D = 0.8$), the model radius exceeds the observed size. We therefore find that the radius constraint for 0509 is fully compatible with the conclusions drawn from the substructure analysis. We stress, however, that this agreement should be interpreted as a broad consistency check rather than evidence that the M1010 model at $t_D = 0.7$ uniquely or definitively describes 0509.

5. DISCUSSION

In this work, we delve deeper into the study by Mandal et al. (2025) on the identification of the explosion mechanism and progenitor properties of Type Ia SNRs. Using numerical models of Type Ia SNRs that exploded via the double detonation (DD) mechanism, we compute the typical size of turbulent substructures in such SNRs. In addition to confirming that iron-dominated substructures are considerably larger than sulfur-dominated substructures in DD SNe (as found by Mandal et al. 2025), we show that these substructure sizes are sensitive to the carbon-oxygen core mass and the helium shell mass of the progenitor WD.

We apply these results to the substructure size distributions in the SNR 0509-67.5, computed from high resolution MUSE observations. We infer spherical wavenumbers corresponding to the typical sulfur-dominated and iron-dominated substructures in SNR 0509-67.5 to be $l_0^S = 31 \pm 2$ and $l_0^{\text{Fe}} = 22 \pm 1$, respectively. These values correspond to characteristic substructure sizes of approximately $\approx 5\%$ (sulfur-dominated) and $\approx 7\%$ (iron-dominated) of the remnant radius (see section 3.3 for discussion on conversion from angular harmonics to length scales). As mentioned earlier, this is a key signature of a sub- M_{ch} WD progenitor for Type Ia SNRs. Our study thus provides novel and independent evidence to the suggestion that SNR 0509 originated from the double detonation of a sub- M_{ch} CO WD (Das et al. 2025). In addition, our suite of SNR models based on DD SN models by Gronow et al. (2021) spanning a range of WD core mass and shell mass helps us constrain the core and shell masses of the progenitor of SNR 0509-67.5. The progenitor is found to be the most consistent

with a WD of core mass and shell mass of $1M_{\odot}$ and $0.05M_{\odot} < M \lesssim 0.1M_{\odot}$, respectively. The total ejecta mass and energy ($\approx 1.5 \times 10^{51}$ ergs) of this model is found to be in good agreement with the prediction of Seitenzahl et al. (2019).

As noted in Section 1, 0509 is also associated with a 1991T-like event based on light echo reconstruction of spectra (Rest et al. 2008). These events are typically overluminous and exhibit slow photometric decline rates. The M1010 model considered here shows broadly similar properties, with high maximum absolute bolometric magnitude ($M_{\text{bol,max}} \sim -19.4$) and relatively slow decline rates ($\Delta m_{15,\text{bol}} \sim 0.96$) along some viewing directions (see Fig. 6 of Gronow et al. 2021). Despite this qualitative similarity, detailed light curve calculations indicate that this model does not reproduce the observed light curve of SN 1991T (Collins et al. 2022). Nevertheless, recent non-LTE radiative transfer calculations suggest that double detonation models may be capable of producing light curves and spectra consistent with both normal and overluminous Type Ia SNe (Shen et al. 2021; Collins et al. 2025). In this context, O’Brien et al. (2024) argue that 1991T-like SNe may represent an extension of the normal Type Ia population, differing primarily in elemental abundances and ionization structure.

Observations have also begun to reveal individual 1991T-like events with signatures potentially consistent with helium shell detonations. For example, SN 2022joj shows shallow Si II absorption features characteristic of the 1991T subclass and has been interpreted as a possible helium-shell double detonation event (Liu et al. 2023). Modeling of this object suggests a helium shell mass in the range $\simeq 0.04\text{--}0.1M_{\odot}$, comparable to the shell masses inferred in this work. Another example is SN 2020eyj (Kool et al. 2023), which initially exhibited a typical 1991T-like spectrum and light curve before later showing evidence for interaction with helium-rich circumstellar material (CSM). Such behavior may be related to the broader connection between 1991T-like SNe and SNe Ia-CSM noted by Leloudas et al. (2015), who argue that some 1991T-like events may arise in systems that produce dense CSM through mass loss from a non-degenerate companion. It is important to note that CSM interaction in these systems typically mani-

fest within the first ~ 100 days of the SN evolution and is not necessarily expected in the remnant phase. The relatively low ambient densities inferred for SNR 0509 therefore do not conflict with the possibility of early-time CSM interaction in some 1991T-like events.

Recent observations of SNR 0509 itself may indicate a helium-enriched environment. Das et al. (2026, in review) report elevated He/H abundance ratios in Balmer-dominated filaments of 0509, pointing to a helium-rich progenitor environment. While the origin of this enrichment remains uncertain (see Das et al. 2026 for more discussion of possible progenitor scenarios), it is broadly consistent with scenarios involving a white dwarf with a substantial helium layer prior to explosion, as inferred from our analysis.

As of now, no explosion models can completely explain the observed features of 1991T-like SNe due to inherent multidimensional nature of the explosion (Pakmor et al. 2024). Given the growing line of evidence that SNR 0509-67.5 originated from a double detonation (Seitenzahl et al. 2019; Das et al. 2025, and this work), we encourage future works on the double detonation model to investigate the effects of multidimensionality and non-LTE on their lightcurves and spectra, as well as study the connection between 1991T-like events and double detonation SN models with dense CSM.

ACKNOWLEDGMENTS

We thank the anonymous referee, whose careful scrutiny significantly improved this manuscript. This work made use of the Heidelberg Supernova Model Archive (HESMA), <https://hesma.h-its.org>. Numerical calculations were performed on the Rivanna computing cluster at University of Virginia. P.G. acknowledges support from the Maryland Space Grant Consortium and NASA.

Software: Sprout (Mandal & Duffell 2023), VisIt (Childs et al. 2012), SHTOOLS (Wieczorek & Meschede 2018), NumPy (Harris et al. 2020), Matplotlib (Hunter 2007), Astropy.

REFERENCES

- Aleo, P. D., Malanchev, K., Sharief, S., et al. 2023, ApJS, 266, 9
- Arévalo, P., Churazov, E., Zhuravleva, I., Hernández-Monteagudo, C., & Revnivtsev, M. 2012, MNRAS, 426, 1793
- Arnett, W. D. 1969, Ap&SS, 5, 180

- Arnett, W. D., Truran, J. W., & Woosley, S. E. 1971, *ApJ*, 165, 87
- Arunachalam, P., Hughes, J. P., Hovey, L., & Eriksen, K. 2022, *ApJ*, 938, 121
- Bacon, R., Accardo, M., Adjali, L., et al. 2010, in *Ground-based and Airborne Instrumentation for Astronomy III*, Vol. 7735, SPIE, 131–139
- Badenes, C., Borkowski, K. J., Hughes, J. P., Hwang, U., & Bravo, E. 2006, *ApJ*, 645, 1373
- Badenes, C., Hughes, J. P., Cassam-Chenaï, G., & Bravo, E. 2008, *ApJ*, 680, 1149
- Bora, Z., Könyves-Tóth, R., Vinkó, J., et al. 2024, *PASP*, 136, 094201
- Bozzetto, L. M., Filipović, M. D., Urošević, D., Kothes, R., & Crawford, E. J. 2014, *MNRAS*, 440, 3220
- Chandrasekhar, S. 1931, *ApJ*, 74, 81
- Chevalier, R. A., Blondin, J. M., & Emmering, R. T. 1992, *ApJ*, 392, 118
- Chevalier, R. A., & Klein, R. I. 1978, *ApJ*, 219, 994
- Childs, H., Brugger, E., Whitlock, B., et al. 2012, in *High Performance Visualization—Enabling Extreme-Scale Scientific Insight (Chapman and Hall/CRC)*, 357–372
- Collins, C. E., Gronow, S., Sim, S. A., & Röpke, F. K. 2022, *MNRAS*, 517, 5289
- Collins, C. E., Shingles, L. J., Sim, S. A., et al. 2025, *MNRAS*, 538, 1289
- Das, P., Seitzzahl, I. R., Ruitter, A. J., et al. 2025, *Nature Astronomy*, doi:10.1038/s41550-025-02589-5
- DES Collaboration, Abbott, T. M. C., Acevedo, M., et al. 2024, *ApJL*, 973, L14
- Duffell, P. C., & MacFadyen, A. I. 2011, *ApJS*, 197, 15
- Ferrand, G., Tanikawa, A., Warren, D. C., et al. 2022, *ApJ*, 930, 92
- Ferrand, G., Warren, D. C., Ono, M., et al. 2019, *ApJ*, 877, 136
- . 2021, *ApJ*, 906, 93
- Filippenko, A. V., Richmond, M. W., Matheson, T., et al. 1992, *ApJL*, 384, L15
- Fink, M., Hillebrandt, W., & Röpke, F. K. 2007, *A&A*, 476, 1133
- Fink, M., Röpke, F. K., Hillebrandt, W., et al. 2010, *A&A*, 514, A53
- Flörs, A., Spyromilio, J., Taubenberger, S., et al. 2020, *MNRAS*, 491, 2902
- Freudling, W., Romaniello, M., Bramich, D., et al. 2013, *A&A*, 559, A96
- Gal-Yam, A. 2017, in *Handbook of Supernovae*, ed. A. W. Alsabti & P. Murdin, 195
- Ghavamian, P., Blair, W. P., Sankrit, R., Raymond, J. C., & Hughes, J. P. 2007, *ApJ*, 664, 304
- Ghavamian, P., Seitzzahl, I. R., Vogt, F. P. A., et al. 2017, *ApJ*, 847, 122
- Gronow, S., Collins, C. E., Sim, S. A., & Röpke, F. K. 2021, *A&A*, 649, A155
- Hansen, C. J., & Wheeler, J. C. 1969, *Ap&SS*, 3, 464
- Harris, C. R., Millman, K. J., van der Walt, S. J., et al. 2020, *Nature*, 585, 357
- Helder, E. A., Kosenko, D., & Vink, J. 2010, *ApJL*, 719, L140
- Hillebrandt, W., Kromer, M., Röpke, F. K., & Ruitter, A. J. 2013, *Frontiers of Physics*, 8, 116
- Hovey, L., Hughes, J. P., & Eriksen, K. 2015, *ApJ*, 809, 119
- Hunter, J. D. 2007, *Computing in Science & Engineering*, 9, 90
- Ivanova, L. N., Imshennik, V. S., & Chechetkin, V. M. 1974, *Ap&SS*, 31, 497
- Ivezić, Ž., Kahn, S. M., Tyson, J. A., et al. 2019, *ApJ*, 873, 111
- Iwamoto, K., Brachwitz, F., Nomoto, K., et al. 1999, *ApJS*, 125, 439
- Kepler, S. O., Kleinman, S. J., Nitta, A., et al. 2007, *MNRAS*, 375, 1315
- Khokhlov, A. M. 1991a, *A&A*, 245, 114
- . 1991b, *A&A*, 245, L25
- Kirshner, R. P. 2010, in *Dark Energy: Observational and Theoretical Approaches*, ed. P. Ruiz-Lapuente, 151
- Kochanek, C. S., Shappee, B. J., Stanek, K. Z., et al. 2017, *PASP*, 129, 104502
- Kolmogorov, A. 1941, *Akademiia Nauk SSSR Doklady*, 30, 301
- Kool, E. C., Johansson, J., Sollerman, J., et al. 2023, *Nature*, 617, 477
- Kosenko, D., Vink, J., Blinnikov, S., & Rasmussen, A. 2008, *A&A*, 490, 223
- Kromer, M., Ohlmann, S., & Röpke, F. K. 2017, *Mem. Soc. Astron. Italiana*, 88, 312
- Lach, F., Röpke, F. K., Seitzzahl, I. R., et al. 2020, *A&A*, 644, A118
- Law, N. M., Kulkarni, S. R., Dekany, R. G., et al. 2009, *PASP*, 121, 1395
- Leloudas, G., Hsiao, E. Y., Johansson, J., et al. 2015, *A&A*, 574, A61
- Liu, C., Miller, A. A., Boos, S. J., et al. 2023, *ApJ*, 958, 178
- Livne, E. 1990, *ApJL*, 354, L53
- Lopez, L. A., Ramirez-Ruiz, E., Huppenkothen, D., Badenes, C., & Pooley, D. A. 2011, *ApJ*, 732, 114
- Mandal, S., & Duffell, P. C. 2023, *The Astrophysical Journal Supplement Series*, 269, 30
- Mandal, S., Duffell, P. C., Polin, A., & Milisavljevic, D. 2023, *ApJ*, 956, 130

- . 2024, *ApJ*, 972, 87
- Mandal, S., Torres-Albà, N., Badenes, C., & Mohamed, S. 2025, arXiv e-prints, arXiv:2508.10752
- Maoz, D., & Graur, O. 2017, *ApJ*, 848, 25
- Niemeyer, J. C., Hillebrandt, W., & Woosley, S. E. 1996, *ApJ*, 471, 903
- Niemeyer, J. C., & Woosley, S. E. 1997, *ApJ*, 475, 740
- Nomoto, K. 1982, *ApJ*, 253, 798
- Nomoto, K., Saio, H., Kato, M., & Hachisu, I. 2007, *ApJ*, 663, 1269
- Nomoto, K., Thielemann, F. K., & Yokoi, K. 1984, *ApJ*, 286, 644
- O’Brien, J. T., Kerzendorf, W. E., Fullard, A., et al. 2024, *ApJ*, 964, 137
- Pakmor, R., Kromer, M., Röpke, F. K., et al. 2010, *Nature*, 463, 61
- Pakmor, R., Kromer, M., Taubenberger, S., et al. 2012, *ApJL*, 747, L10
- Pakmor, R., Seitzzahl, I. R., Ruiter, A. J., et al. 2024, *A&A*, 686, A227
- Perley, D. A., Fremling, C., Sollerman, J., et al. 2020, *ApJ*, 904, 35
- Phillips, M. M. 1993, *ApJL*, 413, L105
- Phillips, M. M., & Burns, C. R. 2017, in *Handbook of Supernovae*, ed. A. W. Alsabti & P. Murdin, 2543
- Phillips, M. M., Ashall, C., Burns, C. R., et al. 2022, *ApJ*, 938, 47
- Phillips, M. M., Ashall, C., Brown, P. J., et al. 2024, *ApJS*, 273, 16
- Polin, A., Duffell, P., & Milisavljevic, D. 2022, *The Astrophysical Journal Letters*, 940, L28
- Polin, A., Nugent, P., & Kasen, D. 2019, *ApJ*, 873, 84
- . 2021, *ApJ*, 906, 65
- Rest, A., Suntzeff, N. B., Olsen, K., et al. 2005, *Nature*, 438, 1132
- Rest, A., Matheson, T., Blondin, S., et al. 2008, *ApJ*, 680, 1137
- Röpke, F. K. 2017, in *Handbook of Supernovae*, ed. A. W. Alsabti & P. Murdin, 1185
- Röpke, F. K., Kromer, M., Seitzzahl, I. R., et al. 2012, *ApJL*, 750, L19
- Ruiter, A. J., & Seitzzahl, I. R. 2025, *A&A Rv*, 33, 1
- Scalzo, R. A., Ruiter, A. J., & Sim, S. A. 2014, *MNRAS*, 445, 2535
- Seitzzahl, I. R., Cescutti, G., Röpke, F. K., Ruiter, A. J., & Pakmor, R. 2013, *A&A*, 559, L5
- Seitzzahl, I. R., Ghavamian, P., Laming, J. M., & Vogt, F. P. A. 2019, *PhRvL*, 123, 041101
- Seitzzahl, I. R., Meakin, C. A., Townsley, D. M., Lamb, D. Q., & Truran, J. W. 2009, *ApJ*, 696, 515
- Seok, J. Y., Koo, B.-C., & Onaka, T. 2013, *ApJ*, 779, 134
- Shen, K. J., & Bildsten, L. 2014, *ApJ*, 785, 61
- Shen, K. J., Blondin, S., Kasen, D., et al. 2021, *ApJL*, 909, L18
- Sim, S. A., Röpke, F. K., Hillebrandt, W., et al. 2010, *ApJL*, 714, L52
- Soker, N. 2025, *The Open Journal of Astrophysics*, 8, 36
- Springel, V. 2010, *MNRAS*, 401, 791
- Taubenberger, S. 2017, in *Handbook of Supernovae*, ed. A. W. Alsabti & P. Murdin, 317
- Tiwari, V., Graur, O., Fisher, R., et al. 2022, *MNRAS*, 515, 3703
- Torres, S., Rebassa-Mansergas, A., Camisassa, M. E., & Raddi, R. 2021, *MNRAS*, 502, 1753
- Truelove, J. K., & McKee, C. F. 1999, *ApJS*, 120, 299
- Vogt, F. P., Álvarez, J. L., Calia, D. B., et al. 2018, *A&A*, 618, L7
- Vogt, F. P. A., Bonaccini Calia, D., Hackenberg, W., et al. 2017, *Phys. Rev. X*, 7, 021044
- Warren, D. C., & Blondin, J. M. 2013, *MNRAS*, 429, 3099
- Warren, J. S., & Hughes, J. P. 2004, *ApJ*, 608, 261
- Weilbacher, P. M., Palsa, R., Streicher, O., et al. 2020, *A&A*, 641, A28
- Wieczorek, M. A., & Meschede, M. 2018, *Geochemistry, Geophysics, Geosystems*, 19, 2574
- Woosley, S. E., & Weaver, T. A. 1994, *ApJ*, 423, 371